Mon. Not. R. Astron. Soc. **287,** 57–68 (1997)

Two modes of gas flow in a single barred galaxy

Peter Englmaier and Ortwin Gerhard
Astronomisches Institut, Universität Basel, Venusstrasse 7, CH-4102 Binningen, Switzerland

Accepted 1996 December 11. Received 1996 November 18; in original form 1996 August 12

ABSTRACT

We investigate stationary gas flows in a fixed, rotating barred potential. The gas is assumed to be isothermal with an effective sound speed c_s, and the equations of motion are solved with smoothed particle hydrodynamics (SPH). Since the thermal energy in cloud random motions is negligible compared with the orbital kinetic energy, no dependence of the flow on c_s is expected. However, this is not the case when shocks are involved.

For low values of c_s an open, off-axis shock flow forms that is characteristic for potentials with an inner Lindblad resonance (ILR). Through this shock the gas streams inwards from x_1- to x_2-orbits. At high sound speeds the gas arranges itself in a different, on-axis shock flow pattern. In this case, there is no gas on x_2-orbits, demonstrating that the gas can behave as if there were no ILR. The critical effective sound speed dividing the two regimes is in the range of values observed in the Milky Way.

We give a heuristic explanation for this effect. A possible consequence is that star formation may change the structure of the flow by which it was initiated. Low-mass galaxies should predominantly be in the on-axis regime.

A brief comparison of our SPH results with those from a grid-based hydrodynamic code is also given.

Key words: hydrodynamics – shock waves – ISM: kinematics and dynamics – galaxies: ISM – galaxies: spiral.

1 INTRODUCTION

Gas kinematic observations in the best-studied barred galaxies imply highly non-circular gas motions. Some examples are NGC 5383 (Duval & Athanassoula 1983), NGC 7496 (Pence & Blackman 1984b), NGC 1365 (Teuben et al. 1986), and our Galaxy (Liszt & Burton 1980; Binney et al. 1991). These non-circular motions are believed to be associated with shocks; large velocity gradients in support of this interpretation have been observed in NGC 6221 (Pence & Blackman 1984a), NGC 1365 (Lindblad & Jörsäter 1987) and NGC 3095 (Weiner, Williams & Sellwood 1993). The shocks can be traced on optical images by the dust lanes that mark swept-up dense gas at the leading edges of the bar (Pence & Blackman 1984a; Athanassoula 1992). In IC 342, millimetre observations of the molecular gas distribution and velocity field suggest that the gas in the shock ridges is falling into the nucleus (Ishizuki et al. 1990). Some estimates for the resulting mass infall rates are ~ 0.01–$0.1\,M_\odot\,yr^{-1}$ in our Galaxy (Gerhard & Binney 1993) and $\sim 4\,M_\odot\,yr^{-1}$ in NGC 7479 (Quillen et al. 1995). The infalling gas may settle on an inner ring and fuel starburst activity (Ishizuki et al. 1990; Kenney et al. 1992).

Because the effective temperature (cloud velocity dispersion) of the gas is much smaller than any orbital velocities, it is generally a good approximation to think of quasi-stationary galactic gas flows in terms of the periodic orbits in the underlying gravitational potential, so long as these periodic orbits do not cross. Many hydrodynamic simulations using a variety of numerical techniques have confirmed this (Sanders & Huntley 1976; Schwarz 1981, 1984; Combes & Gerin 1985; Habe & Ikeuchi 1985; van Albada 1985; Mulder & Liem 1986; Athanassoula 1992; Friedli & Benz 1993; Jenkins & Binney 1994). When the periodic orbits do cross or intersect, then pressure or viscous forces must always become important and ensure that the gas streamlines match together to form a well-defined flow pattern. This typically happens near the orbital resonances of the system, and it is here that shocks are found to form.

The geometrical structure, the extent, and the strength of these shocks depend on a variety of external parameters. Most important is whether the gravitational potential has an inner Lindblad resonance (ILR) and hence a family of x_2-orbits, but also the strength and axial ratio of the bar are significant parameters (Roberts, van Albada & Huntley 1979; Sanders & Tubbs 1980; Athanassoula 1992).

We have begun a study aimed at obtaining a better understanding of these gas flows, and using them as tracers for the dynamical properties of our Galaxy and barred galaxies in general. We have used a two-dimensional smoothed particle hydrodynamics (SPH) method, based on the SPH-code of Steinmetz & Müller (1993)

which Matthias Steinmetz kindly made available. The extent to which the interstellar medium (ISM) in galaxies can be modelled by simple gas dynamics has been discussed recently by Sellwood & Wilkinson (1993) and Binney & Gerhard (1993). In the present study, we have omitted the self-gravity of the fluid, treating it as a tracer; the restriction to two dimensions is in order to increase the resolution. Later, the SPH method will allow us to study the effect of the self-gravity of the gas, particularly in the high-density regions that generally form in these flows.

In the course of this work, we have found that the shock properties in barred potentials also depend on internal parameters used to model the gas: specifically, on the sound speed if the gas is assumed to be an isothermal fluid. This paper reports on these results. We first describe the mass model, initial conditions, etc. (Section 2), and give some details on the numerical method (Section 3). In Section 4 we show that both off-axis and on-axis shocks may form in a potential with an ILR, study the influence of some relevant parameters, and briefly compare our results with those from grid-based simulations. Finally, in Section 5 we discuss some implications of our main result.

2 DESCRIPTION OF THE MODELS

In this paper we consider gas flows in galaxy models with a given gravitational potential for the stellar component, as detailed in Section 2.1. Our assumptions concerning the initial conditions, the hydrodynamics of the gas, and a simple gas recycling law for mimicking star formation are given in Sections 2.2–2.4, while the numerical method (SPH) is briefly described in Section 3.

2.1 Mass models for the stellar component

In order to be able to compare our results from SPH with those from a hydrodynamic grid method, we have adopted the analytic family of models from Athanassoula (1992). These models include a bulge, disc, and bar component. The bulge follows a Hubble profile

$$\rho(r) = \rho_b(1 + r^2/r_b^2)^{-3/2}, \tag{1}$$

and the stellar disc is a simple Kuzmin–Toomre disc with surface density

$$\Sigma_d(R) = \frac{R_d M_d}{2\pi}(R^2 + R_d^2)^{-3/2}. \tag{2}$$

The parameters are chosen such as to give an approximately flat rotation curve: $R_d = 14.1$ kpc, $M_d = 2.3 \times 10^{11}$ M$_\odot$, $r_b = 0.33$ kpc, and $\rho_b = 23.6$ M$_\odot$ pc^{-3}.

The bar component is modelled as a simple Ferrers ellipsoid with density

$$\rho(X) = \begin{cases} \rho_F(1 - g^2) & \text{for } g^2 < 1, \\ 0 & \text{elsewhere,} \end{cases} \tag{3}$$

with $g^2 = X^2/a_F^2 + (Y^2 + Z^2)/b_F^2$ and parameters $a_F = 5$ kpc, $b_F = 2$ kpc. We have considered two values for the bar mass: one is specified by setting $\rho_F = 0.4476$ M$_\odot$ pc^{-3} (Model A, corresponding to Athanassoula's model 001), the other has one-half that mass (our standard Model S). To place the L1-Lagrange point at $r_{L1} = 6.0$ kpc, we chose a pattern speed of $\Omega_p = 35.3$ km s^{-1} kpc^{-1} for the Model A bar and $\Omega_p = 32.0$ km s^{-1} kpc^{-1} for the Model S bar. This corresponds to bar rotation periods of 0.174 and 0.192 Gyr, respectively. Then from the $m = 0$ component of the potential, the corotation radius is $R_{CR} = 5.8$ kpc in both cases.

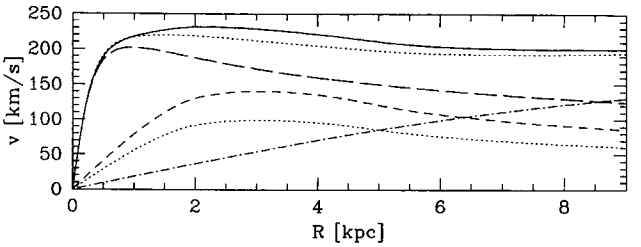

Figure 1. Circular rotation curves in the equatorial plane: total (full and dotted lines) for Models A and S, and contributions from the bulge (long-dashed), Ferrer's bar (short-dashed for Model A, dotted for Model S), and disc (dash-dotted).

The rotation curves for both models and the contributions of the individual components (from the respective $m = 0$ components of the gravitational force in the equatorial plane) are shown in Fig. 1.

2.2 Initial conditions and symmetry

In the present two-dimensional calculations the gas is initially set up on circular orbits with constant surface density $\Sigma_0 = 1$ M$_\odot$ pc^{-2}. Outside some radius r_{cut} beyond corotation the density is set to a constant, i.e. the pressure gradients are set to zero.

The non-axisymmetric part of the potential is turned on gradually within a time τ_{on} equal to approximately one-half the rotation period of the bar. After continuing the calculation for some time t given in Table 1, the gas flow is nearly stationary in the rotating frame.

In these calculations we have assumed point symmetry with respect to the origin. This effectively doubles the number of particles, and increases the resolution by a factor of $\sqrt{2}$. We have checked that the results in simulations without the assumed point symmetry are essentially identical.

2.3 Gas dynamics

For the gas we have assumed an isothermal equation of state with an

Table 1. Parameters for the models computed. For all runs we used $N \approx 2 \times 10^4$ particles in two dimensions and imposed point symmetry, giving a mean resolution length of $h \lesssim 0.1$ kpc. All simulations are rotating clockwise. Table columns give (1) model designation, (2) effective sound speed of the gas, (3) whether gas recycling was used, (4) constant determining the individual particle sizes, cf. Section 3, and (5) time since start of the calculation for which results are reported.

Model	c_s[km/s]	Gas recycl.	ζ	t[Gyr]
S-1	10	no	1.2	0.6
S-2	15	no	1.2	0.6
S-3	20	no	1.2	0.6
S-4	25	no	1.2	0.6
S-5	30	no	1.2	0.6
S-6	15	yes	1.2	0.6
S-7	20	yes	1.2	0.6
A-1	10	no	1.8	0.4
A-2	15	yes	1.2	0.6
A-3	20	yes	1.2	0.6

effective sound speed c_s, representing the random motions in the interstellar cloud medium. This approach is consistent with the ISM model of Cowie (1980), who argued that the cloud fluid can be treated like an isothermal gas if the clouds have an equilibrium mass spectrum. The equlibrium is assumed to be maintained by a steady supply of small clouds by supernovae. Using SPH as described in the next section we are thus solving the Euler equations

$$\frac{\mathrm{D}\boldsymbol{v}}{\mathrm{D}t} = \frac{\partial \boldsymbol{v}}{\partial t} + (\boldsymbol{v}\cdot\nabla)\boldsymbol{v} = -c_s^2 \frac{\nabla\Sigma}{\Sigma} - \nabla\phi \tag{4}$$

for effective sound speeds of $c_s = 10 - 30\,\mathrm{km\,s^{-1}}$.

2.4 Gas recycling

Because the gas loses angular momentum to the stellar bar by gravitational torques, a substantial accretion rate towards the centre develops. In run S-1, for example, at a radius of 1 kpc, the accretion rate is approximately $7.6\times10^6\,\mathrm{M_\odot\,Gyr^{-1}}$, and in S-5 it is $\sim1.9\times10^7\,\mathrm{M_\odot\,Gyr^{-1}}$, rising continuously with sound speed between these two cases. For comparison, for our initial surface density of $1\,\mathrm{M_\odot\,pc^{-2}}$ the total gas mass inside corotation is $1.06\times10^8\,\mathrm{M_\odot}$. Thus after ~5–15 Gyr all of the gas would have been accreted to the centre. To avoid this, we have in some of our models introduced a gas recycling law which takes away gas in high-density regions and adds material uniformly over the disc:

$$\mathrm{d}\Sigma/\mathrm{d}t = \alpha\Sigma_0^2 - \alpha\Sigma^2. \tag{5}$$

This may crudely be thought of as simulating star formation in dense regions and mass loss from pre-existing bulge and disc stars. The star formation rate α is taken to be $0.3\,\mathrm{M_\odot^{-1}\,pc^2\,Gyr^{-1}}$. Equation (5) includes a quadratic Schmidt (1959) law and a constant source term, but the functional form was mainly chosen to be able to compare with the grid-based simulations of Athanassoula (1992).

3 NUMERICAL METHOD

We have used a two-dimensional SPH method to solve the hydrodynamical equations for the gas flow in the galaxy equatorial plane. Restricting the calculation to two dimensions increases greatly the resolution we can achieve, and this is important in the present problem for resolving the shocks that dominate the evolution. Since we are interested in isothermal shocks, we are assuming implicitly that the gas can cool rapidly. We then expect that the gas can expand vertically with speeds only of the order of the sound speed. Since this is much smaller than the dynamical velocities, vertical motions cannot affect the shock front even if this has finite width (such as one or two cloud mean free paths). The gas will also only marginally be able to expand out of a three-dimensional layer within a dynamical time; hence the expansion of the post-shock gas cannot lead it too far above the downstream material that it will meet next. Thus we expect the two-dimensional description to be a reasonable approximation. Notice that it is not possible to test this rigorously with three-dimensional simulations of this particle number, unless anisotropic particles are used; for, to resolve the disc vertically, one needs to make it substantially thicker than in reality, which increases the vertical escape times. We have done some such three-dimensional simulations; in these the observed gas flows were indeed similar to the two-dimensional ones.

As there are many variants of SPH (see the reviews of Benz 1990 and Monaghan 1992), we give a short overview of our code, which is based on the code of Steinmetz & Müller (1993). A few details on how the method works will be useful for interpreting the results reported below. SPH solves the equations of motion by a Monte Carlo integration. The integration points are not drawn by random, but are the positions of the particles, as they happen to be. Ideally the particles should be distributed in a glass-like structure to minimize numerical errors. Apart from this the particles have no physical meaning. The forces on each parcel of fluid can be calculated by smearing out the properties of the particles over a few mean particle distances.

For constant smoothing length h, the smoothing is done by folding each field quantity A such as temperature or pressure with the kernel function $W(\boldsymbol{r})$:

$$\langle A(\boldsymbol{r})\rangle = \int A(\boldsymbol{r}')W(\boldsymbol{r}'-\boldsymbol{r},h)\mathrm{d}^2x' + O(h^2)$$
$$\approx \sum_i \frac{m_i}{\Sigma_i} A_i W(\boldsymbol{r}_i - \boldsymbol{r}, h). \tag{6}$$

Here A_i and Σ_i are evaluated at the position of particle i. Thus the surface density is approximated by

$$\langle\Sigma(\boldsymbol{r})\rangle = \sum_i m_i W(\boldsymbol{r}_i - \boldsymbol{r}, h). \tag{7}$$

Only structure on scales larger than a few resolution lengths h is meaningful. We used the spline kernel

$$W(\boldsymbol{r}-\boldsymbol{r}',h) = \frac{W_0}{h^2}\begin{cases} 1-\frac{3}{2}u^2+\frac{3}{4}u^3 & 0\le u \le 1,\\ \frac{1}{4}(2-u)^3 & 1<u\le 2,\\ 0 & u>2,\end{cases} \tag{8}$$

with $u = |\boldsymbol{r}-\boldsymbol{r}'|/h$, and the constant W_0 is determined from the normalization condition

$$1 = \int W(\boldsymbol{r},h)\mathrm{d}^2x. \tag{9}$$

The kernel describes the surface density distribution of one particle.

To increase resolution in high-density regions the particles are assigned individual smoothing lengths

$$h_i = \zeta\sqrt{m_i/\Sigma_i} \tag{10}$$

with $\zeta = 1.2$ in most cases (see Table 1). In this case, the field quantities at particle positions $\boldsymbol{r}_i$ are evaluated with the symmetrized kernel

$$W(\boldsymbol{r}_i - \boldsymbol{r}_j, h_i, h_j) = \tfrac{1}{2}\{W(\boldsymbol{r}_i - \boldsymbol{r}_j, h_i) + W(\boldsymbol{r}_i - \boldsymbol{r}_j, h_j)\} \tag{11}$$

to ensure momentum conservation. This symmetrized kernel is also used in the calculation of the surface density $\Sigma_i = \langle\Sigma(\boldsymbol{r}_i)\rangle$ at particle position $\boldsymbol{r}_i$. To evaluate the field quantity at an arbitrary position $\boldsymbol{r}$ the original kernel (8) is used.

We have used the following simple approximation for adjusting the particle smoothing length:

$$h_i^{(n+1)} = \sqrt{\frac{N_0}{N_i^{(n)}}}\,h_i^{(n)}. \tag{12}$$

Here $N_0 = 4\pi\zeta^2$ is the desired number of neighbours within $2h_i$, and $N_i^{(n)}$ the recorded number of neighbours of particle i in the nth time step. This ensures that the number of neighbours of a particle is approximately independent of time and of its location. In our case with strong shocks the original method used by Steinmetz & Müller (1993) was found to result in a larger number of neighbours in the shock region and a loss in resolution. In some cases we also observed large oscillations in the particle size from time step to time step when a particle entered the shock.

The Euler equations in SPH read

$$\frac{\mathrm{d}\boldsymbol{v}_i}{\mathrm{d}t} = -\sum_j m_j \left(\frac{P_i}{\Sigma_i^2} + \frac{P_j}{\Sigma_j^2} + Q_{ij}\right) \nabla_i W(\boldsymbol{r}_i - \boldsymbol{r}_j, h_i, h_j) - \nabla\phi_i, \tag{13}$$

where Q_{ij} is an artificial viscosity tensor (Monaghan & Gingold 1983):

$$Q_{ij} = \begin{cases} \dfrac{-\alpha c_s \mu_{ij} + \beta \mu_{ij}^2}{\Sigma_{ij}} & (\boldsymbol{r}_i - \boldsymbol{r}_j)\cdot(\boldsymbol{v}_i - \boldsymbol{v}_j) \le 0, \\ 0 & \text{otherwise}, \end{cases} \tag{14}$$

$$\mu_{ij} = \frac{h_{ij}(\boldsymbol{r}_i - \boldsymbol{r}_j)\cdot(\boldsymbol{v}_i - \boldsymbol{v}_j)}{(\boldsymbol{r}_i - \boldsymbol{r}_j)^2 + \eta^2}, \tag{15}$$

with $\alpha = 1$, $\beta = 2$, $\eta = 0.1h_{ij}$, $h_{ij} = (h_i + h_j)/2$, and $\Sigma_{ij} = (\Sigma_i + \Sigma_j)/2$. The quantity μ_{ij} is an approximation for the contribution of the particle pair (i,j) to the local volume compression $h\,\nabla\cdot\boldsymbol{v}$ over one resolution length h.

The artificial viscosity actually consists of two contributions. The term with the constant α corresponds to the bulk viscosity, whereas the term with the constant β corresponds to the von Neumann–Richtmyer viscosity. Both correspond to a 'viscous pressure' in the Euler equation, namely $\alpha\Sigma c_s |h\,\nabla\cdot\boldsymbol{v}|$ and $\beta\Sigma(h\,\nabla\cdot\boldsymbol{v})^2$ (Benz 1990). The von Neumann–Richtmyer viscosity is necessary to simulate strong shocks because it guarantees causality by transporting information with signal speed $\sqrt{\beta}|h\,\nabla\cdot\boldsymbol{v}|$ across the shock fronts (e.g. the flow is supersonically compressed ($c_s < -h\,\nabla\cdot\boldsymbol{v}$). The bulk viscosity is used to damp post-shock oscillations.

As reported by Hernquist & Katz (1989), the artificial viscosity tensor does not vanish in pure shear flows. Therefore some authors use the modified artificial viscosity tensor proposed by Balsara (1995):

$$\tilde{Q}_{ij} = Q_{ij}\tfrac{1}{2}(f_i + f_j) \tag{16}$$

with

$$f_i = \frac{|\langle\nabla\cdot\boldsymbol{v}\rangle_i|}{|\langle\nabla\cdot\boldsymbol{v}\rangle_i| + |\langle\nabla\times\boldsymbol{v}\rangle_i| + 0.0001c_s/h_i}. \tag{17}$$

The effect of this is to reduce the viscosity in regions with large values of $|\langle\nabla\times\boldsymbol{v}\rangle_i|$. However, we have not found this viscosity switch useful in the presence of shocks with strong shear. In a sheared shock, both the divergence and the rotation of the velocity field become large, thus the f_i decrease below unity and the viscosity becomes too small to treat the shocks adequately.

The gas recycling law (5) is realized by adjusting the mass of each particle m_i at its individual time step $n+1$ according to

$$m_i^{(n+1)} = m_i^{(n)} + \mathrm{d}t_i \frac{\mathrm{d}m}{\mathrm{d}\Sigma}\frac{\mathrm{d}\Sigma}{\mathrm{d}t} = m_i^{(n)} + \mathrm{d}t_i \left(\frac{h_i}{\zeta}\right)^2 \alpha(\Sigma_0^2 - \Sigma_i^2). \tag{18}$$

The particle velocities are kept constant.

4 RESULTS

4.1 Off-axis shocks at low sound speeds

Fig. 2 shows the distribution of gas particles, the velocity field and the underlying orbital structure in Model S-2. This model describes an isothermal fluid with a sound speed $c_s = 15\,\mathrm{km\,s^{-1}}$. The velocity field was calculated on a regular grid, using the SPH smoothing algorithm, and is shown in a rotating frame in which the bar and the gas flow pattern are approximately stationary.

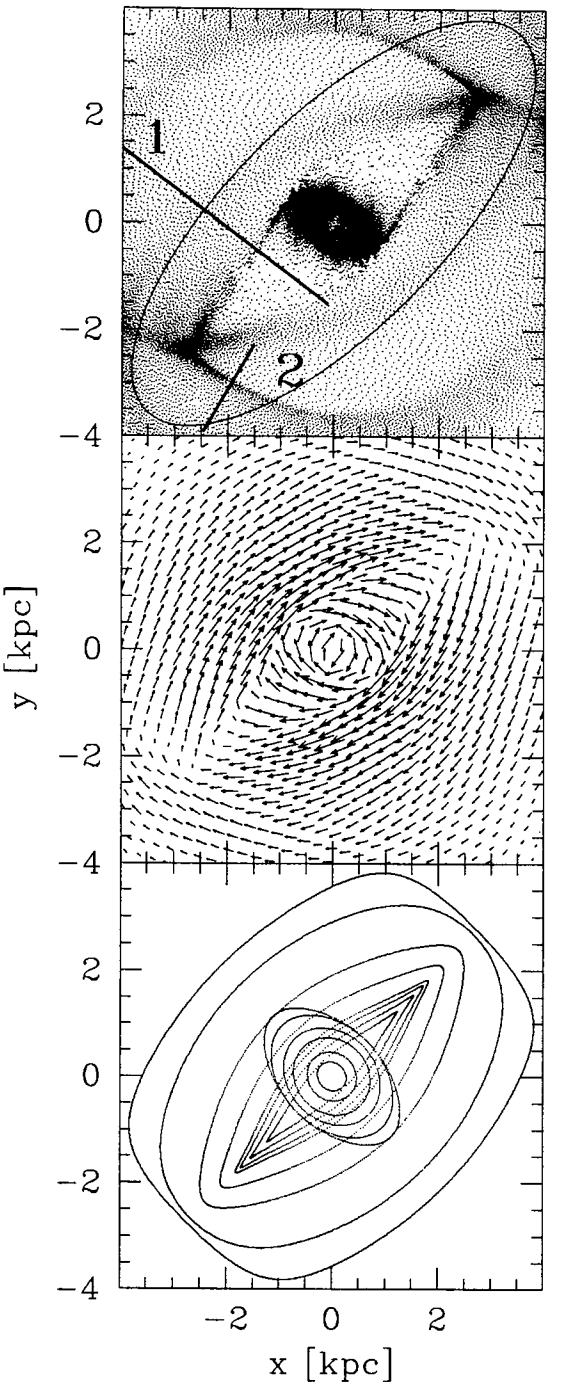

Figure 2. Top: Particle distribution in Model S-2, for time $t = 0.6$ Gyr. The outline of the bar is given by the ellipse. Middle: The corresponding velocity field. Bottom: Some x_1- and x_2-orbits that are useful for the interpretation of the gas flow.

As is well-known, the flow is influenced strongly by the families of periodic orbits in the underlying potential and the transitions between them. The most important families here are the x_1-orbits elongated along the bar and the central x_2-orbits oriented perpendicular to the bar. The outermost orbits shown in

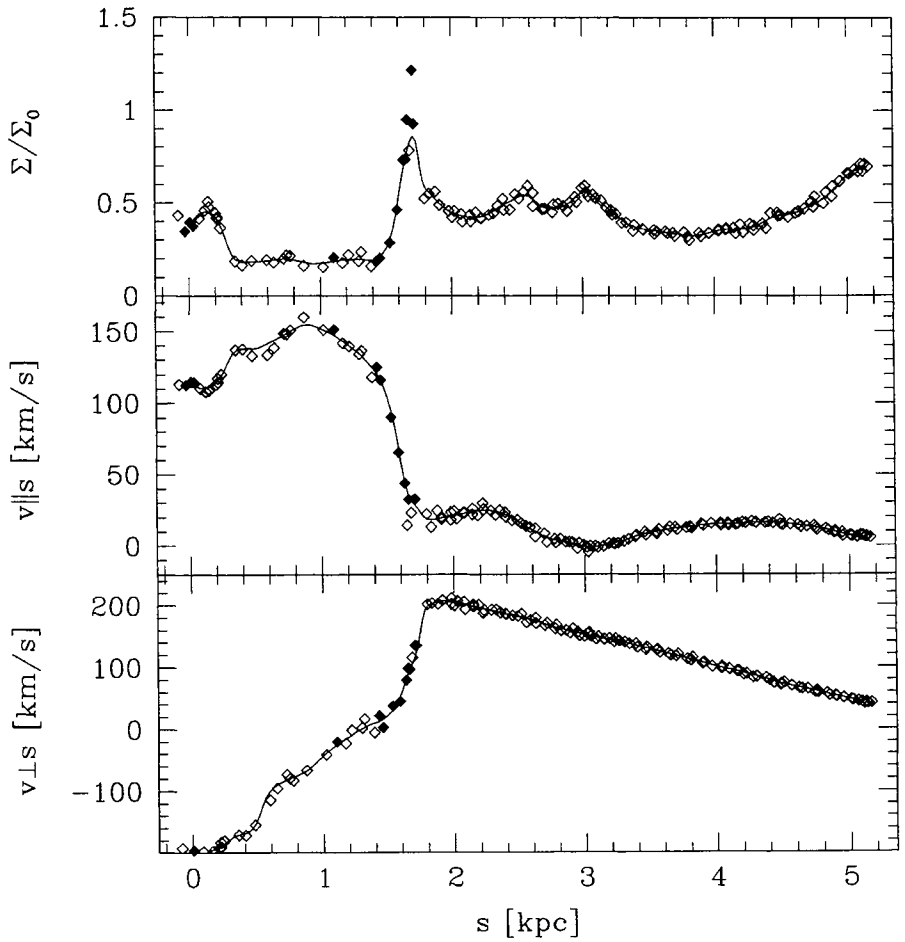

Figure 3. Surface density (top), velocity $v_{\|s}$ along (middle), and velocity $v_{\perp s}$ perpendicular to (bottom) 'Slit 1' in Fig. 2, for all particles within one smoothing length h of the slit. This slit intersects the cusped orbit shock approximately perpendicularly. The diamonds give the surface density Σ_i evaluated at the positions of individual particles; the solid line shows the smoothed SPH value along the slit computed by integrating over all overlapping particles. Full symbols denote particles that are decelerated in the shock, i.e. are compressed supersonically: $-h\nabla\cdot\boldsymbol{v} > c_s$.

the bottom panel of Fig. 2 belong to a 4/1-resonant family. See Contopoulos & Papayannopoulos (1980) for this notation.

The velocity field shows that the gas occupies x_1-orbits in the main bar region and then shifts gradually to x_2-orbits in the inner parts. In this process it forms a shock along the leading edges of the bar; in model S-2 the shock starts at ≈3.7 kpc and continues inward with a small inclination angle with respect to nearby x_1-orbits. From a particle point of view, the gas particles moving through the shock exchange momentum with particles downstream to avoid penetration of each other.

The gas moves inwards alongside the shock and then swings around the disc of x_2-orbits towards the symmetric far-side branch of the shock. The flow follows the x_2-orbits some way around the centre, reaches a density maximum and opens like a spray as some particles go into the disc, whereas others move outward again into the far-side shock. With lower orbital energy, they then begin another half-revolution. The gas thus loses further orbital energy and spirals inwards in a few revolutions until it joins the gas on the outer occupied x_2-orbits. The resulting central ring of dense gas is often called the x_2-disc.

Gas coming into the bar region from outside encounters a trailing spiral shock wave which occurs at the intersection of colliding streams on the outer x_1-orbits and the 4/1-orbit family. In Model S-2 this shock front starts on the major axis at ≈3.7 kpc where the x_1-family meets the 4/1-family. For definiteness, we call the two types of shock the 'cusped-orbit shock' and the '4/1-spiral shock'.

Fig. 3 shows the density and the velocities of particles within one smoothing length h of 'Slit 1' plotted in Fig. 2. The left side of Fig. 3 with small s corresponds to the low-density, pre-shock region inside the cusped orbit. The top panel shows the gas surface density through the cusped orbit shock along the slit. The points give the surface density Σ_i evaluated at the positions of individual particles; the solid line shows the smoothed SPH value along the slit computed by integrating over all overlapping particles [cf. equation (7)]. As determined from the latter, the density jump across the shock is about a factor of 2; because of resolution effects this is a lower limit. The rise of the density from its pre-shock value occurs on a length-scale comparable to the smoothing length h; here h is approximately 140 pc upstream, 70 pc at the density peak and 90 pc downstream. The post-shock region (near the peak of the density) appears still not resolved; most of the right side of the diagram shows densities on streamlines which are quite unrelated to the shock (see Fig. 2).

The lower two panels of Fig. 3 show the gas velocities $v_{\|s}$ and $v_{\perp s}$ parallel and perpendicular to the 'slit' direction in the top panel of Fig. 2. At the shock surface $v_{\|s}$ is approximately the velocity with which a supersonic collision occurs; $v_{\perp s}$ is approximately the transverse shear component of the streaming velocity. It is seen that $v_{\|s}$ jumps by $\sim 100\,\mathrm{km\,s^{-1}}$ over the same length-scale over

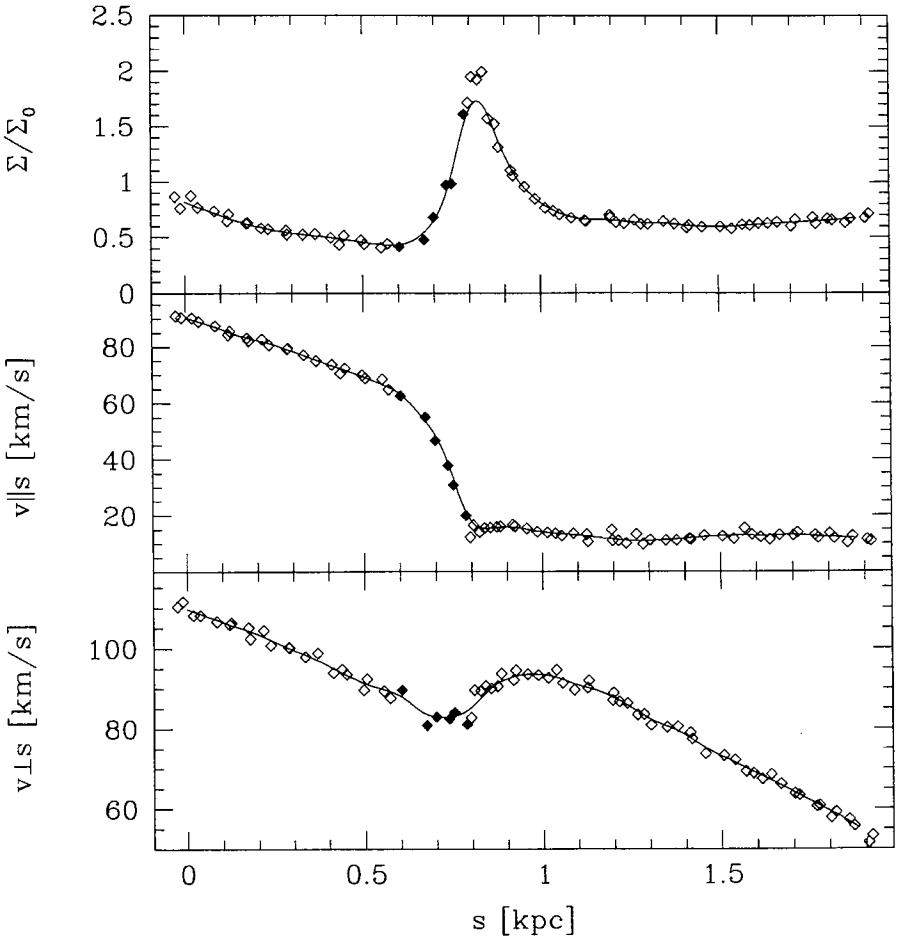

Figure 4. As Fig. 3, but for 'Slit 2' through the 4/1-spiral shock in Fig. 2.

which the density jump occurs. The filled symbols in Fig. 3 denote those particle positions at which $-h\nabla\cdot\boldsymbol{v} > c_s$ – the local criterion for a shock to take place. For a simple non-shearing, isothermal shock the Rankine–Hugoniot jump conditions predict $v_{\|s,pre} \times v_{\|s,post} = c_s^2$; hence for $\Delta v_{\|s} \simeq 100\,\mathrm{km\,s^{-1}}$ and $c_s = 15\,\mathrm{km\,s^{-1}}$ one finds $v_{\|s,pre} \simeq 102\,\mathrm{km\,s^{-1}}$ and $v_{\|s,post} \simeq 2\,\mathrm{km\,s^{-1}}$ for the upstream pre-shock and downstream post-shock components, which appears approximately correct. The corresponding density jump is a factor of 50 and must then be clearly unresolved.

However, from the lower panel of Fig. 3 and also from the middle panel of Fig. 2 we see that the gas flow in this region has a strong shear component and there is likely also a discontinuity in the transverse $v_{\perp s}$ velocity across the shock. Quantitatively, $\Delta v_{\perp s} \simeq 180\,\mathrm{km\,s^{-1}}$ across the unresolved shock width. In this case, the jump conditions are not as simple (Syer & Narayan 1993).

Fig. 4 shows analogous information for the 4/1-spiral shock. This shock is less complicated because shear velocities are seen only in the post-shock region, but are essentially absent in the shock region itself. The density goes up by a factor of 4, and the Mach number $M = v_{\|s}/c_s$ also jumps by a factor of 4. From the Rankine–Hugoniot conditions we would expect $\rho_{pre}/\rho_{post} = 1/M^2$, so the maximum density is again unresolved.

4.2 On-axis shocks at high sound speeds

So far we have adopted a sound speed of $c_s = 15\,\mathrm{km\,s^{-1}}$ which is consistent with observations of the turbulent speed of clouds in the ISM. However, the observed values in the Galactic disc do vary, so it is interesting to see whether the stationary flow pattern depends on c_s or not.

From a theoretical point of view we might expect several regimes to occur between two extreme cases: in the limit of negligible sound speed every slight compression of the gas causes a shock and an isothermal fluid would become effectively incompressible; in the other limit of high sound speeds no shocks can form at all.

Indeed, we found that there are two qualitatively different quasi-stationary gas flow solutions in the potentials investigated. The transition between these two configurations is shown in Fig. 5. At low sound speeds, the gas flow is as described in the last section. At higher sound speeds ($c_s \simeq 25$–$30\,\mathrm{km\,s^{-1}}$ in our standard potential with circular velocity $\approx 200\,\mathrm{km\,s^{-1}}$) the x_2-orbits are no longer occupied and a cusped orbit shock cannot form; instead, it is replaced by a broken shock configuration near the long axis of the bar. This structure resembles more the shocks that Athanassoula (1992) found to occur in barred potentials with no inner Lindblad resonance (ILR), while of course the potential used still has an ILR. The spiral wave also is no longer strong enough to form a 4/1-spiral shock.

A heuristic explanation for these results is as follows. Consider a sequence of models such as in Fig. 5, starting with a case with well-developed off-axis shocks. The speed with which the spray of gas inside the cusped orbit meets the cusped orbit shock decreases

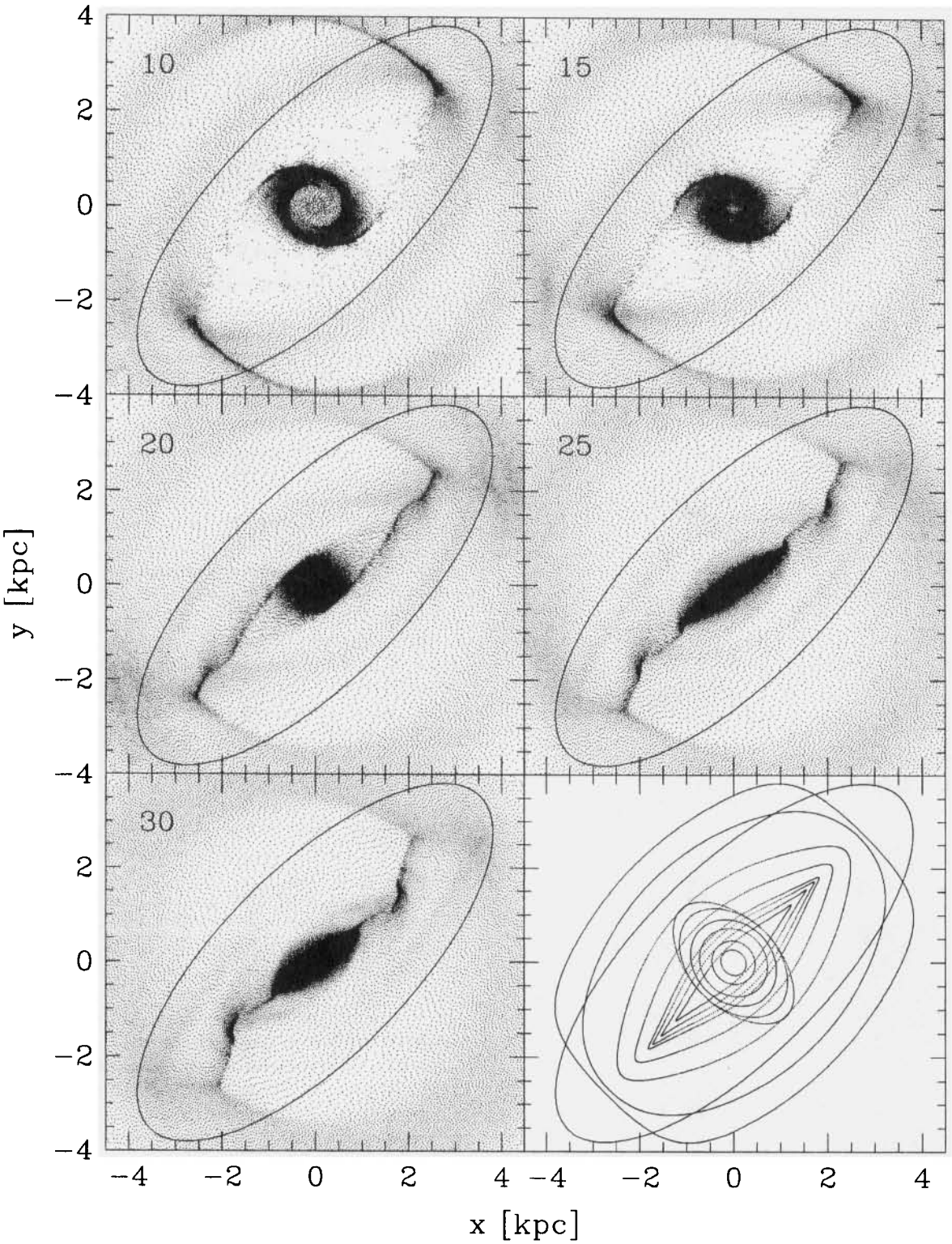

Figure 5. A sequence of models with increasing sound speed as indicated in the upper left corner of each panel (models S-1 to S-5 in Table 1). Between 20 and 25 km s^{-1} the flow pattern changes as described in the text. The orbital structure in all the simulations is the same; some closed orbits are shown in the lower right panel.

outwards (Fig. 2, middle). Thus the shock front should end where the velocity $v_{\parallel s}$ in the shock frame becomes smaller than the sound speed. When the sound speed is increased while keeping the potential constant, the streaming velocities will to first order remain unchanged, so that the shock front must move inwards. This means that it must move towards x_1-orbits deeper in the potential well and closer to the major axis. The second aspect is the gas inflow along the shock which feeds gas on to the x_2-ring. As the shock front moves closer to the bar major axis, the inflowing gas will eventually no longer be able to settle on x_2-orbits. Once

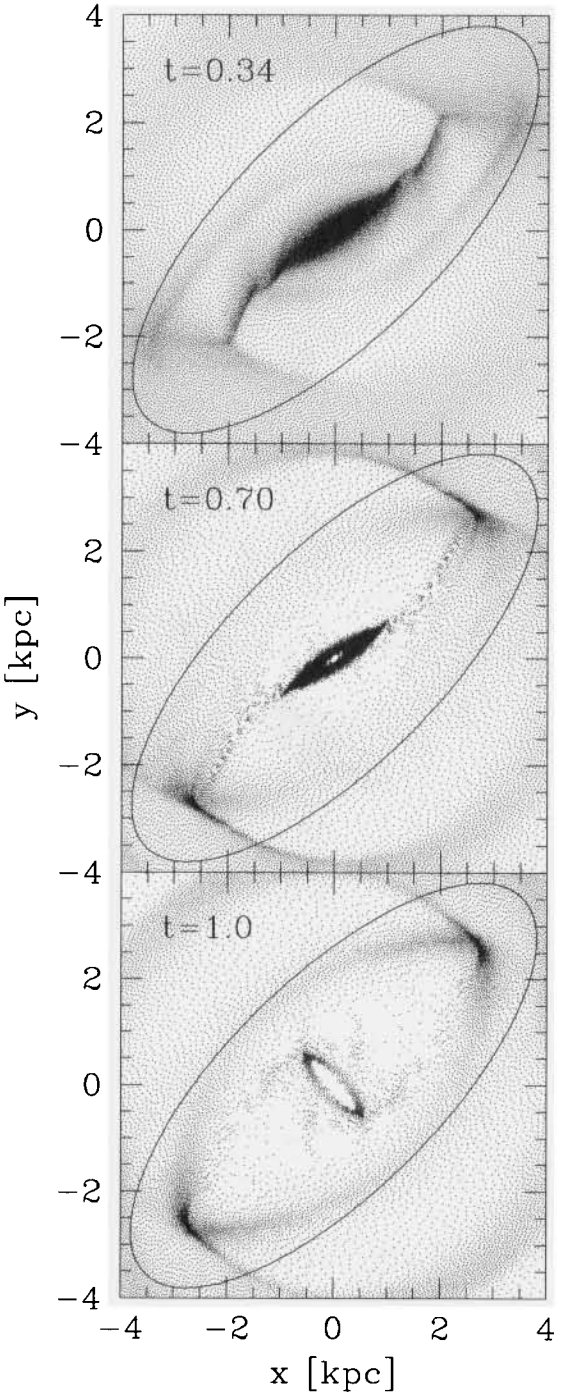

Figure 6. An on-axis shock solution switches to an off-axis shock flow when the sound speed is changed by hand and the massive central x_1-disc is removed. Times are specified in Gyr and the bar rotation period is 0.174 Gyr.

x_1-orbits cannot be occupied, one of the principal factors instrumental in building up the off-axis shock has disappeared.

From Fig. 5, we conclude that the transition between both solutions in terms of the variation of c_s is more or less continuous. E. Athanassoula (private communication) has also found in her grid simulations the existence of two distinct gas flow patterns; however, she appears to see a very sharp transition at a critical sound speed of $c_s = (16.4 \pm 0.1)$ km s^{-1} (in the potential model A). It is not clear at present precisely which aspects of the numerical schemes are responsible for this difference; nor whether any of these schemes describes the dynamics of the ISM accurately enough to say how the real ISM behaves in this respect.

An interesting aspect of the flow patterns at high sound speed is that the gas inflow still forms a central disc; however, this now consists of gas on x_1-orbits rather than x_2-orbits. This is only possible because in our Ferrers bar potential the x_1-orbits are not self-intersecting. If they did self-intersect, a still different flow pattern connected with strong accretion to the centre would likely result.

4.3 Influence of initial situation

We now ask whether the type of shock structure that develops in the simulation depends on the initial gas configuration as well as on the sound speed. In principle, quasi-stationary gas flows with both types of shock structure might exist in one and the same gravitational potential, and the system could evolve towards one or the other equilibrium, depending on its initial state. To test this, we start a simulation in an extreme initial state where the system is already in quasi-equilibrium such that the flow has formed an on-axis shock structure, and then see whether it evolves to an off-axis shock solution when we reduce the sound speed to 10 km s^{-1}.

When the sound speed is dropped, a shock in the original gas flow must remain a shock. On the other hand, a shallow compression wave may suddenly become supersonic, and the newly forming shock can change the flow pattern in such a way that the original shock structure is modified or disappears. When the sound speed is reduced in the equilibrium flow shown in the top panel of Fig. 6, the main shock front immediately moves away from the bar major axis in the direction of the position where the main off-axis shock would be located in a low-sound-speed model. In addition, new spiral shocks form near the position of the 4/1-resonance, and much of the gas in the inner bar region falls towards the centre, building a massive, elongated x_1-disc. This x_1-disc is massive enough to prevent gas from moving on to x_2-orbits, so no off-axis flow can form, and the whole configuration swings back towards the bar major axis. The resulting quasi-equilibrium is shown in the middle panel of Fig. 6.

We now turn on gas recycling, which essentially removes the high-density material in the x_1-disc. To speed up the computation, we use a higher gas recycling constant, $\alpha = 3\ \mathrm{M}_\odot^{-1}\ \mathrm{pc}^2\ \mathrm{Gyr}^{-1}$, than in the other models. This removes the obstacle in the flow, and after a few more rotations the gas now settles on x_2-orbits and an off-axis shock front has formed. The structure of the inner x_2-disc in the final configuration (bottom panel of Fig. 6) is somewhat different from those shown previously because of the large gas recycling rate.

We draw two conclusions from this experiment. (i) If we release small quantities of gas in a barred potential, then independently of the initial velocity field the flow pattern adjusts itself to that which is natural for gas at this sound speed in this gravitational potential. This is because the velocity field of the gas that evolved towards the final off-axis configuration in Fig. 6 must have been close to the velocity field typical for on-axis flows. (ii) On the other hand, a massive disc set up previously is hard to perturb, and may prevent the incoming gas flow from taking up its natural flow pattern. In real galactic discs, such massive discs are expected to form stars and be depleted of gas; thus eventually we expect the gas there to return to its preferred configuration.

4.4 Influence of gas recycling and bar mass

In Fig. 7 we compare models with different sound speeds and bar

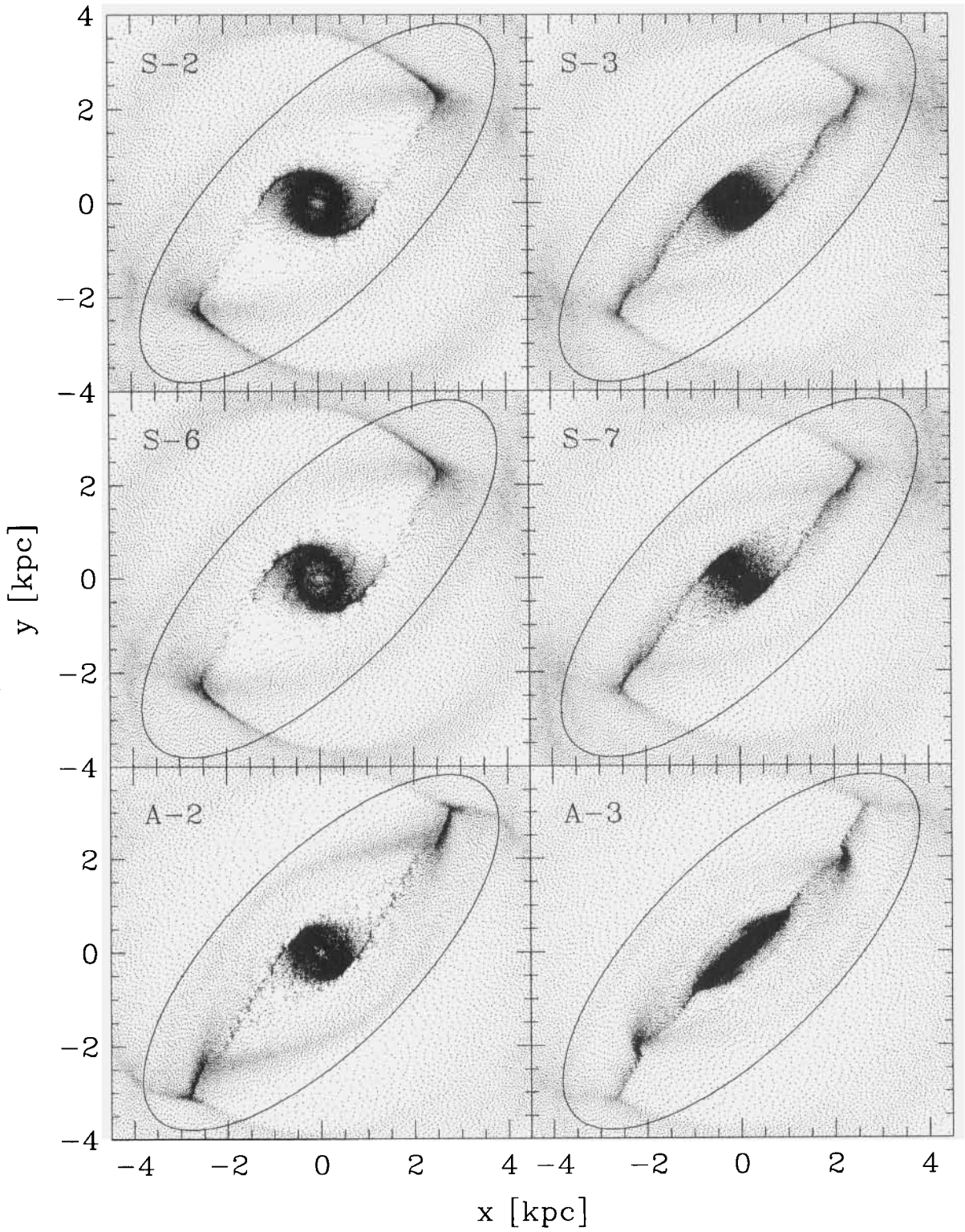

Figure 7. Influence of bar mass, sound speed and gas recycling on the gas flow pattern. Models in the left-hand panels have sound speed $c_s = 15\,\mathrm{km\,s^{-1}}$, those in the right-hand panels $c_s = 20\,\mathrm{km\,s^{-1}}$. The upper two panels show gas flows in the standard potential and without gas recycling that mimics star formation, the middle two panels show gas flows in the standard potential with gas recycling, and the lower two panels are for a potential with a bar twice as massive as before and again include gas recycling. See Table 1 for parameters. There is no influence of gas recycling on the flow pattern, but a stronger bar or a higher sound speed can drive the gas flow towards a configuration with on-axis shocks.

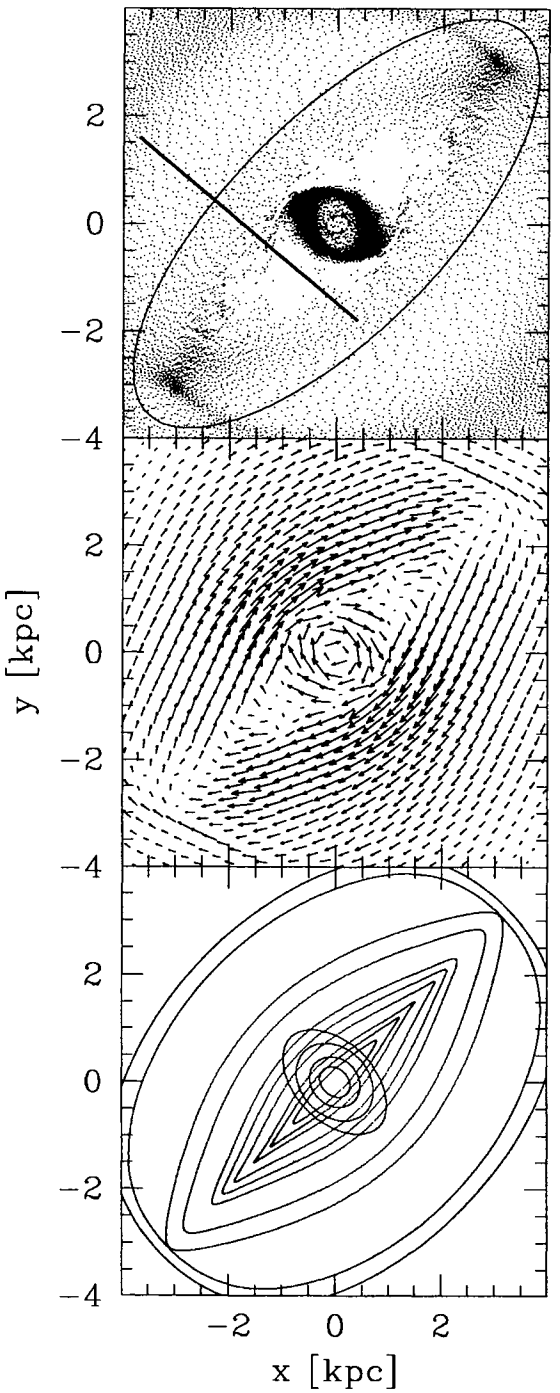

Figure 8. As Fig. 2 for Model A-1 at $t = 0.4$ Gyr. This model is the same as Model 001 of Athanassoula (1992), and the figure should be compared with her fig. 2.

masses, and with or without gas recycling as indicated in the figure caption and Table 1.

First we consider the influence of the gas recycling by comparing Model S-2 with S-6 and Model S-3 with S-7. In both cases the large-scale flow configuration does not change. However, the simulations with gas recycling (S-6 and S-7) look more clumpy; we believe that this is an artefact of having to introduce gas particles with different masses in the gas recycling algorithm.

Between the middle panels and the lower panels of Fig. 7 the bar mass is doubled and therefore the orbits change as well as the resonances. The more massive bar forces more elongated x_1-orbits (see Fig. 8). For the lower sound speed the pattern maintains off-axis shocks, but the shock front now starts nearer to the end of the bar and is closer to the bar major axis. There is also a new large gap in the shock front at $(x, y) = (2, 2)$ kpc.

For the higher sound speed (Model A-3) the flow field in the more massive bar potential has changed to an on-axis configuration. Thus the critical sound speed which divides the two shock patterns appears to decrease for increasing bar mass.

4.5 Comparison of SPH and grid-based results

In Model A-1 we have reproduced model 001 of Athanassoula (1992) to test our code against a grid-based method: in this case, a second-order flux splitting code written by G. D. van Albada (van Albada & Roberts 1981). Both methods solve the Euler equations, thus the same results should be expected. However, differences may arise due to the statistical nature of SPH or the different numerical and artificial viscosities used in both codes. Comparing simulations of the same physical problem computed with both numerical methods may give valuable clues about their reliability.

Fig. 8 shows the particle distribution, gas velocity field, and closed orbit structure for Model A-1. The potential is the same as used for model 001 of Athanassoula (1992), and the initial conditions are set up identically except that the disc is truncated at a smaller radius (6 kpc as opposed to 16 kpc in the grid model). Compared with the simulations discussed earlier, we have used a larger smoothing parameter ($\zeta = 1.8$). The reason for this is that, because of the stronger bar, the gas in this potential moves to the centre more quickly, leaving fewer particles in the shock front in quasi-equilibrium. To measure the shock properties displayed in Fig. 9, it was then necessary to employ more smoothing.

The global structure of the flow seen in Fig. 8 is similar to that of the grid model (see Athanassoula's fig. 2 for comparison). The point on the major axis where the 4/1-spiral shock begins is at the same distance from the centre (at $\simeq$4.3 kpc). The cusped orbit shocks are straight in both simulations; however, in the SPH model they form a smaller angle with the bar major axis than in the grid model.

The shock properties shown in Fig. 9 are similar to Athanassoula's findings (her fig. 11) when we take into account that our and her slits are not at identical positions and that the resolution is different. The shape of the function describing the gas velocity along the slit is very similar, and the maximum upstream value and the downstream velocities agree quantitatively (to be able to make the comparison with Athanassoula, the velocities in the two lower panels of Fig. 9 are measured relative to the inertial frame and include a contribution from the bar rotation). The shock is slightly less well resolved in the SPH simulation, corresponding to a somewhat broader density peak. The peak density is underestimated in both simulations; in the SPH case it is also time-dependent. The value that we measure from Fig. 9 appears to be higher than that in Athanassoula's fig. 11 (the units in both diagrams are $\Sigma_0 = 1\,M_\odot\,pc^{-2}$).

The large scatter in the density plot in Fig. 9 is due to the rather large width of the slit, $4h$. Particularly in the low-density region (upstream, inside the cusped orbit) there are very few particles in the SPH simulation. This is a general resolution problem with SPH: particles follow the gas flow; thus low-density regions near resonances, through which the flow moves rapidly, are often not well-resolved, whereas regions of high density such as the inner x_2-ring contain many more particles than necessary for adequate resolution.

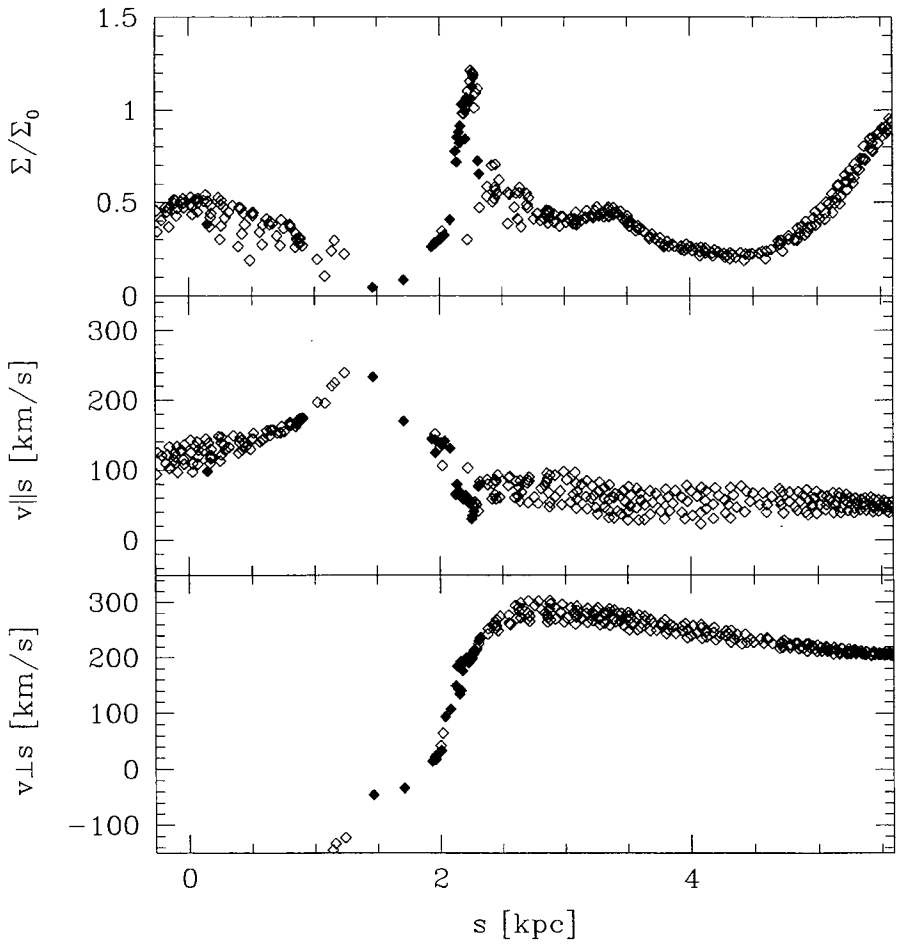

Figure 9. As Fig. 3 for the slit in Fig. 8.

The reader should note that this is even true in a symmetrized 2D simulation with 20 000 particles. In three-dimensional simulations, especially when high density contrasts are present, resolution may be a much more severe problem.

However, as the comparison shows, SPH gives surprisingly accurate solutions in the case at hand. Thus we may confidently move to fully self-gravitating simulations in which the real strengths of SPH will be used.

5 DISCUSSION

We have studied the structure of quasi-stationary shock fronts in realistic barred galaxy models with an ILR, and have found that both off-axis and on-axis shocks can result in the same rotating potential, depending on the sound speed of the isothermal fluid. The off-axis shocks at low sound speeds had previously been assumed to be the rule in such potentials, whereas on-axis shocks had been found in potentials too shallow to have an ILR. We have verified in one case that the gas flow resulting from our two-dimensional SPH simulation agrees approximately with that found in a grid-based simulation of Athanassoula (1992).

If the quasi-equlibrium flow that results in a given galaxy model depends on the fluid parameters in the hydrodynamical calculation – here, the sound speed – then it may equally depend on the entire prescription of modelling the ISM: whether its complicated multi-phase structure is better represented as particle-like or in terms of an ideal fluid. This offers the opportunity of learning about the 'correct' description of interstellar fluids from detailed studies of galactic flows.

The critical sound speed that we have found to divide the two shock regimes is around $\sim 20\,\mathrm{km\,s^{-1}}$ in our standard model potential, which corresponds to a barred galaxy with a circular velocity of $v_c \simeq 200\,\mathrm{km\,s^{-1}}$. It is somewhat lower for a model with a stronger bar. A dependence on bar strength etc. is not surprising, since the occurrence of a shock depends on both the sound speed and the fluid flow velocities in the relevant bar region.

Expressed dimensionlessly, the critical sound speed is ~10 per cent of the circular velocity. This implies that dwarf or Magellanic galaxies should predominantly be in the on-axis regime. This might have important implications for the dependence of morphology on absolute magnitude.

For our Galaxy, the value of $\sim 20\,\mathrm{km\,s^{-1}}$ is in an interesting regime, for, while the cloud velocity dispersion in the Galactic disc inside the solar radius is $\sim 5\,\mathrm{km\,s^{-1}}$ (Clemens 1985), the vertical cloud velocity dispersion in the Galactic bulge region is inferred to be $\sim 25\,\mathrm{km\,s^{-1}}$ (Bally et al. 1988). Moreover, the effective sound speed in the ISM may be higher than the cloud dispersion if magnetic fields contribute significant pressure, as may be expected especially near the Galactic Centre (Morris 1994).

Assuming that our Galaxy is representative, it would thus appear difficult to predict the type of flow pattern that would form in a barred galaxy. It is even unclear whether the flow would find a single quasi-stationary flow configuration. There also arises the possibility that large-scale star formation, by increasing the

turbulent pressure in the disc, might itself change the structure of the flow by which it was initiated. Since the on-axis shock patterns are generally associated with larger mass inflow rates, a starburst changing the pattern from off-axis to on-axis could thereby prolong its own gas supply. One may even speculate that at early times, when star formation rates are generally higher, the morphology of the gas flows could have been systematically shifted towards on-axis shock flows with higher mass accretion rates. If true this would have obvious relevance to *HST* observations of high-redshift galaxies; thus further work in this direction should be useful.

ACKNOWLEDGMENTS

We are grateful to M. Steinmetz for many discussions on SPH and for making his code available. We also thank E. Athanassoula, J. Binney and M. Samland for helpful discussions and suggestions. This work was supported by the Max-Planck-Institut für Astrophysik in Garching, the Landessternwarte Heidelberg, and the Swiss National Science Foundation.

REFERENCES

Athanassoula E., 1992, MNRAS, 259, 345
Bally J., Stark A. A., Wilson R. W., Henkel C., 1988, ApJ, 324, 223
Balsara D. S., 1995, J. Comput. Phys., 121, 357
Benz W., 1990, in Buchler J. R., ed., The Numerical Modelling of Nonlinear Stellar Pulsations. Kluwer, Dordrecht, p. 269
Binney J. J., Gerhard O. E., 1993, in Holt S. S., Verter F., eds, AIP Conf. Proc. 278, Back to the Galaxy. Am. Inst. Phys. New York, p. 87
Binney J. J., Gerhard O. E., Stark A. A., Bally J., Uchida K. I., 1991, MNRAS, 252, 210
Clemens D. P., 1985, ApJ, 295, 422
Combes F., Gerin M., 1985, A&A, 150, 327
Contopoulos G., Papayannopoulos T., 1980, A&A, 92, 33
Cowie L. L., 1980, ApJ, 236, 868
Duval M. F., Athanassoula E., 1983, A&A, 121, 297
Friedli D., Benz W., 1993, A&A, 268, 65
Gerhard O. E., Binney J. J., 1993, in Dejonghe H., Habing H. J., eds, Proc. IAU Symp. 153, Galactic Bulges. Kluwer, Dordrecht, p. 275
Habe A., Ikeuchi S., 1985, ApJ, 289, 540
Hernquist L., Katz N., 1989, ApJS, 97, 231
Ishizuki S., Kawabe R., Ishiguro M., Okumura S. K., Morita K.-I., 1990, Nat, 344, 224
Jenkins A., Binney J. J., 1994, MNRAS, 270, 703
Kenney J. D. P., Wilson C. D., Scoville N. Z., Devereux N. A., Young J. S., 1992, ApJ, 395, L79
Lindblad P. O., Jörsäter S., 1987, in Palous J., ed., Evolution of Galaxies. Czech. Acad. Sciences, Ondrejov, p. 289
Liszt H. S., Burton W. B., 1980, ApJ, 236, 779
Monaghan J. J., 1992, ARA&A, 30, 543
Monaghan J. J., Gingold R. A., 1983, J. Comput. Phys., 52, 374
Morris M., 1994, in Genzel R., Harris A. I., eds, The Nuclei of Normal Galaxies. Kluwer, Dordrecht, p. 185
Mulder W. A., Liem B. T., 1986, A&A, 157, 148
Pence W. D., Blackman C. P., 1984a, MNRAS, 207, 9
Pence W. D., Blackman C. P., 1984b, MNRAS, 210, 547
Quillen A. C., Frogel J. A., Kenney J. D. P., Pogge R. W., DePoy D. L., 1995, ApJ, 441, 549
Roberts W. W., van Albada G. D., Huntley J. M., 1979, ApJ, 233, 67
Sanders R. H., Huntley J. M., 1976, ApJ, 209, 53
Sanders R. H., Tubbs A. D., 1980, ApJ, 235, 803
Schmidt M., 1959, ApJ, 129, 243
Schwarz M. P., 1981, ApJ, 247, 77
Schwarz M. P., 1984, MNRAS, 209, 93
Sellwood J. A., Wilkinson A., 1993, Rep. Prog. Phys., 56, 173
Steinmetz M., Müller E., 1993, A&A, 268, 391
Syer D., Narayan R., 1993, MNRAS, 262, 749
Teuben P. J., Sanders R. H., Atherton P. D., van Albada G. D., 1986, MNRAS, 221, 1
van Albada G. D., 1985, A&A, 142, 491
van Albada T. S., Roberts W. W., 1981, ApJ, 246, 740
Weiner B. J., Williams T. B., Sellwood J. A., 1993, BAAS, 183, #76.07

This paper has been typeset from a TEX/LATEX file prepared by the author.